Journal of Volcanology and Geothermal Research 427 (2022) 107568

Contents lists available at ScienceDirect

Journal of Volcanology and Geothermal Research

journal homepage: www.journals.elsevier.com/journal-of-volcanology-and-geothermal-research

Volcanic unrest at Nevados de Chillán (Southern Andean Volcanic Zone) from January 2019 to November 2020, imaged by DInSAR

Ana Astort [a,*], Gregorio Boixart [a], Andrés Folguera [a], Maurizio Battaglia [b,c]

[a] Instituto de Estudios Andinos, Universidad de Buenos Aires-CONICET, Buenos Aires 1428, Argentina
[b] U.S. Geological Survey, Volcano Disaster Assistance Program, Menlo Park, CA, USA
[c] Department of Earth Sciences, Sapienza - University of Rome, Rome, Italy

ARTICLE INFO

Keywords:
Nevados de Chillán
DInSAR
Eruption cycle
Volcanic unrest
Deformation modeling

ABSTRACT

The volcanic complex of Nevados de Chillán, located in the Southern Volcanic Zone (SVZ) of the Andes, has been active for the past 640 ± 20 ka. Its volcanic activity includes dome forming eruptions, explosive events, and lava flows. The most recent eruption cycle started in January 2016. We employ DInSAR time-series from Sentinel-1 data to investigate the unrest episode from January 2019 to November 2020. Two distinct periods of unrest are recognized in the time series. The first period (from January to October 2019) coincides with explosive events, dome growth inside the active crater, and a decrease in seismic activity but does not present a significant deformation. The second period (October 2019 to November 2020) is characterized by a displacement towards the sensor's line-of-sight of 100–120 mm. The observed surface deformation is compatible with an inflation source approximately 1.5 km south-southwest of the present active vent, at 5.5 ± 0.5 km depth from the surface, and with a volume change of 0.044 ± 0.014 km^3. The most likely explanation for the observed inflation of Nevados de Chillan is the intrusion of magma in a reservoir feeding the current eruption cycle.

1. Introduction

Explosive eruptions from active volcanoes in the Southern Andean Volcanic Zone can seriously impact critical economic areas in Argentina and Chile. The abundant ash fall/flow deposits from these eruptions are a source of soil degradation for decades (e.g., Naranjo and Stern, 1998; Elissondo et al., 2015; Delgado, 2021). Eruptions from the large volcanic complex of Nevados de Chillán are a clear example of this kind of activity. Nevados de Chillán is a group of coalescent stratovolcanoes (3216 m a.s.l, 36.86° S, 71.38° W) in the Ñuble region of south-central Chile. The volcanic complex consists of two main volcanic centers, compositionally distinct (Dixon et al., 1999), situated ~10 km apart, and extends along a north-northwest to south-southeast trending axis with 17 identified craters (Orozco et al., 2016). The northwestern Cerro Blanco subcomplex is dominantly andesitic, while the southeastern Las Termas subcomplex is predominantly dacitic (Dixon et al., 1999; Fig. 1).

The regional geodynamics and stress field is controlled by the oblique subduction of the Nazca plate beneath the South American plate at a rate of approximately 66 mm/yr (~N70°E) (Cembrano and Lara, 2009). Nevados de Chillán presents a north-northwest to south-southeast alignment of cones and emission centers nearly orthogonal to the regional stress. This alignment could be influenced by the northwest Cortaderas Lineament (Ramos and Barbieri, 1989; Ramos and Folguera, 2005; Stanton-Yonge et al., 2016). The lineament extends 200 km towards the foreland in Argentina and has been interpreted as a structural accommodation zone (Radic, 2010).

According to Cembrano and Lara (2009), Nevados de Chillán could be a kinematically uncoupled development, where the plumbing system and the surface volcanic structures are more related to basement structures than the regional stress regime. An important implication would be that the magma-feeding mechanism for Nevados de Chillán might be controlled by quasi-instantaneous extensions along west-northwest trending axes during episodes of crustal relaxation triggered by major earthquakes (Cembrano and Lara, 2009). Nonetheless, field evidence is inconclusive. The 2010 Mw = 8.8 Maule earthquake was not followed by any eruption (Eggert and Walter, 2009; Pritchard et al., 2013; OVDAS report, 2021). Instead, a subsidence pattern up to 12 cm (roughly oriented N-S) was documented from the few ALOS images available for interferometric processing, probably caused by fluid loss and pressure decrease in the underlying hydrothermal reservoirs (Pritchard et al., 2013). Farías et al. (2014) studied the response of Nevados de Chillán to two aftershocks (MW = 6.1 and 7.1) of the 2010

* Corresponding author.
E-mail address: anaastort@gl.fcen.uba.ar (A. Astort).

https://doi.org/10.1016/j.jvolgeores.2022.107568
Received 27 July 2021; Received in revised form 13 April 2022; Accepted 22 April 2022
Available online 28 April 2022

Maule earthquake (MW = 8.8), reporting an increase in local seismic activity after the first aftershock, a sign of reactivation of local structures. Farías and Basualto (2020) concluded that the megathrust of the 2015 Illapel earthquake (MW = 8.3) induced dynamic stress changes in the order of 0.5–1 bar at the Nevados de Chillán that probably lead to an increase in the permeability, allowing high-pressurized fluids to migrate. After a few months the volcanic center experienced several phreatic explosions and a new fissure opened in the active crater.

Nevados de Chillán has been active at least from 640 ± 20 ka with extrusion of subglacial andesite flows, followed by subglacial and subaerial eruption of basaltic andesite to low-silica rhyolite lavas (Fig. 1; Dixon et al., 1999).

The volcanic complex has a history of periodic eruptions of low to medium energy that last for years, with eruptive columns reaching heights of 3 km (Global Volcanism Program, 2013). The Observatorio Volcánico de los Andes del Sur (OVDAS) classifies the activity of Nevados de Chillán as Vulcanian/Subplinian (*https://www.sernageomin.cl/complejo-volcanico-nevados-de-Chillán/*). Violent eruptions can occur, affecting the nearby villages whose economy is based on tourism (Naranjo and Moreno, 2009).

Recorded eruptive episodes date back to the 1861–1865 Santa Gertrudis scoria cone and lava field formation in the Cerro Blanco subcomplex (Petit-Breuilh, 1995; Mee et al., 2006). The latest eruptive activity has been concentrated exclusively in the Las Termas subcomplex (Fig. 1, Farías et al., 2014). Between 2003 and 2008, the Las Termas subcomplex produced several low-magnitude explosive events producing ash columns and lava flows (Naranjo and Lara, 2004; Naranjo and Moreno, 2009; Coppola et al., 2016). In December 2015, this subcomplex experienced an increase in seismicity and energy released by the explosive events. In addition, a new crater was identified in 2016, northeast of the volcano Arrau, created by several phreatic explosions (Fig. 1; OVDAS report, 2021; Orozco et al., 2016). From middle 2017 to present the unrest has been characterized by ash venting, explosions, effusions of lava, growth, and destruction of domes. According to OVDAS, since March 2020, the volcanic activity remains at low energy levels with volcano-tectonic earthquakes (Mw = 4) at a depth around 4 km, sporadic long-period events associated with subsurface fluid flow, and small lava/pyroclastic flows (OVDAS report, 2021).

GNSS data recorded from 2015 to 2020 (Cardona et al., 2021) evidenced an uplift event beginning in July 2019, coinciding with the eruption of several lava flows from August to December 2019. The composition of gas samples acquired during early 2016 and middle of 2017 indicated that the gas emitted had its origin in the exsolution from melt at high temperature (>850 °C), evidence that a new shallow intrusion of magma was taking place (Moussallam et al., 2018).

In this work, we use DInSAR to investigate the deformation between January 2019 and November 2020 (see Appendix A and Appendix B). We show evidence of a large swelling deformation that we interpret as the recharge of a magma reservoir feeding the present eruption cycle. The deformation imaged by processing DInSAR ascending and descending orbits show a correlation between ground deformation and eruptive episodes. According to our modeling results, the observed deformation field is produced by the recharge of magmatic reservoir beneath the Las Termas subcomplex, orientated along the main geologic structures of the volcanic system (see Cembrano and Lara, 2009; Pritchard et al., 2013; Farías et al., 2014; Farías and Galván, 2019).

2. Radar data

2.1. Processing

The SAR dataset consists of 15 ascending (orbit 91) and 57 descending (orbit 83) radar images from the Sentinel-1 catalogue (European Space Agency, C-Band, available online at https://www.copernicus.eu/en/accessing-data-where-and-how/conventional-data-access-hubs), from January 2019 to November 2020 (Appendix A and Appendix B). To enhance the coherence quality of the interferograms, we discarded satellite data collected in June, July, August, and September,

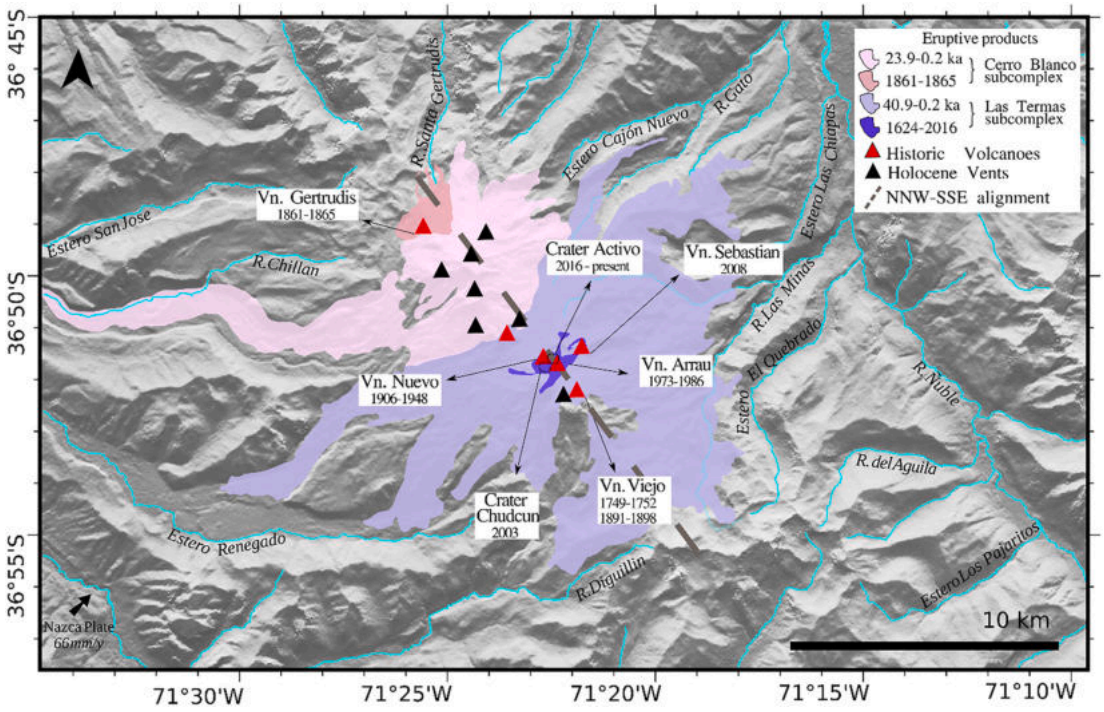

Fig. 1. The volcanic complex of Nevados de Chillán. The Cerro Blanco subcomplex extends northwest (light purple) and the Las Termas subcomplex southeast (purple). Magmatic products from 40 ka until present are represented by different colored areas. From 1700 until present, volcanic activity (red triangles) had been mostly concentrated in the Las Termas subcomplex with multiple eruptions occurring in some of the intervals shown. The gray dashed line corresponds to the alignment of cones and craters, which is interpreted as the trace of the Chillán-Cortaderas fault. (For interpretation of the references to colour in this figure legend, the reader is referred to the web version of this article.)

because of the large amount of snow accumulated on the slopes of the volcanic complex. The descending satellite data were acquired with an acquisition frequency of 6 days and the ascending data with a frequency of 12 days with a gap between May 2019 and March 2020 (Table 1). These two datasets have been acquired in TOPS mode with an interferometric wide (IW) beam. TOPS mode collects data from a swath of 250 km with a spatial resolution of 14.1 × 2.3 m in azimuth and range, respectively. The product type is Single Look Complex (SLC) (*https://sentinel.esa.int/web/sentinel/missions/sentinel-1*).

The interferograms were processed using GMTSAR, an open source InSAR Processing System based on the Generic Mapping Tools (Sandwell et al., 2011a, 2011b). This software has modules that implement the DInSAR Small Baseline Subsets (SBAS) technique and atmospheric correction.

The first step of alignment and co-registration of the complete set of images was accomplished with the geometric approach described by Xu et al. (2017). Then, date pairs for the generation of interferograms were selected by minimizing the spatial baseline and maximizing the numbers of pairs by relaxing the temporal baseline. Only 15 scenes were available in the Sentinel-1 catalogue for the period January 2019 to December 2020 for ascending orbits. Therefore, only 68 interferograms were generated considering the temporal and spatial baselines of 450 days and 100 m (Fig. 2a). Two hundred and sixty-four (264) interferograms were generated from the 57 descending scenes, considering pairs with 210 days and 50 m for the temporal and spatial baselines (Fig. 2b).

We used a digital elevation model (SRTM) of 3-arc *sec* (~90 m resolution) for the topographic correction, and precise Sentinel-1 orbits for the Earth's curvature correction for interferograms flattening. Once the interferograms were created, we applied a Gaussian filter of 200 m and decimation of 8° in range and 2° in the azimuth direction. For the unwrapping procedure, a coherence mask with a threshold of 0.3 was considered when computing the Snaphu code which is included as a module in GMTSAR (Chen and Zebker, 2002). A bilinear polynomial trend was fitted, and then subtracted to each unwrapped interferogram, to reduce long atmospheric wavelength noise and possible residual orbital. An area of approximately 100·100 pixels, with no deformation inside each unwrap map, was used as a stable reference for the processing (Figs. 3 and 4).

2.2. SBAS time-series

Time series from all the generated interferograms were processed by the SBAS time-series approach with a smoothing parameter of 1, and 3 iterations for the atmospheric correction included in the process (Berardino et al., 2002). This approach allowed a proper spatial and temporal characterization of the deformation patterns within the studied area and time-period.

Significant noise from the atmospheric effect is visible in most interferograms because of the high altitude of the volcanic complex. The atmospheric noise comes from stratifications of the atmosphere correlated with topography and turbulent atmospheric events. We applied the atmospheric correction with common-point stacking between nearby scene grids to mitigate this noise (Tymofyeyeva and Fialko, 2015; Xu et al., 2017). The common-point stacking is performed during the SBAS time-series estimation under the assumptions of slow deformation changes in time, and atmospheric noise randomly distributed in time. It compares interferograms with an equal time span that share a common scene, and therefore share the same phase delay due to atmospheric noise (Tymofyeyeva and Fialko, 2015). The atmospheric phase noise (APS) estimated for each scene, and the corresponding displacement grids with and without atmospheric correction applied, can be observed in Figs. A1–A6 in Appendix A.

Displacement time-series and maps of cumulative displacements per year are presented in Figs. 3 and 4. Considering the discontinuities in the availability of images from ascending orbits (Fig. 3), the cumulative displacement per year was calculated in different periods for each

Table 1
Scenes and perpendicular baselines for 57 descending and 15 ascending scenes processed in this paper (Appendix A and Appendix B). The date format corresponds to yyyymmdd and the perpendicular baseline $\boldsymbol{B}_{perp}$ length is in meters.

Descending Scenes	B_{perp} [m]	Ascending Scenes	B_{perp} [m]	Descending Scenes	B_{perp} [m]	Ascending Scenes	B_{perp} [m]
20190106	−105.17	–	–	20191208	−63.98	–	–
20190112	26.2	20190112	89.34	20191214	−27.03	–	–
20190118	−54.79	–	–	20200113	−19.34	–	–
20190124	−61.7	20190124	49.91	20200119	−27.28	–	–
20190130	−28.72	–	–	20200131	−25.17	–	–
20190205	−47.04	20190205	−5.25	20200212	−2.46	–	–
20190211	−28.14	–	–	20200218	−35.01	–	–
20190217	−65.65	20190217	11.43	20200224	−52.06	–	–
20190223	−12.95	–	–	20200301	−38.73	–	–
20190301	−22.44	–	–	20200307	−63.06	20200307	−15.45
20190307	−18.81	–	–	20200313	−2.39	–	–
20190313	−19.34	20190313	68.55	20200319	−29.13	20200319	0.00
20190319	−82.88	–	–	20200325	−62.88	–	–
–	–	–	–	–	–	20200331	23.64
20190325	−50.86	20190325	47.38	20200406	−95.69	20200406	−62.55
20190331	−19.78	–	–	–	–	20200412	48.94
20190406	−59.42	20190406	−60.91	20200424	−77.52	20200424	3.82
20190412	−93.27	–	–	20200430	−44.49	–	–
–	–	20190418	−22.28	20200506	−127.34	–	–
20190424	−3.92	–	–	20200512	−100	–	–
20190430	−25.71	20190430	−35.21	20200518	−133.52	–	–
20190506	−122.88	–	–	20200524	−103.48	–	–
20190512	−82.31	–	–	20200530	−56.36	–	–
20190518	−106.8	–	–	20200605	−201.06	–	–
20190524	−67.63	–	–	20200611	−102.68	–	–
20190530	−72.51	–	–	20201027	−39.8	–	–
20191027	−134.55	–	–	20201102	−84.87	–	–
20191102	0	–	–	20201108	12.76	–	–
20191108	−49.63	–	–	20201120	25.5	–	–
20191114	−40.67	–	–	20201126	−69.04	–	–
20191120	46.33	–	–	–	–	–	–

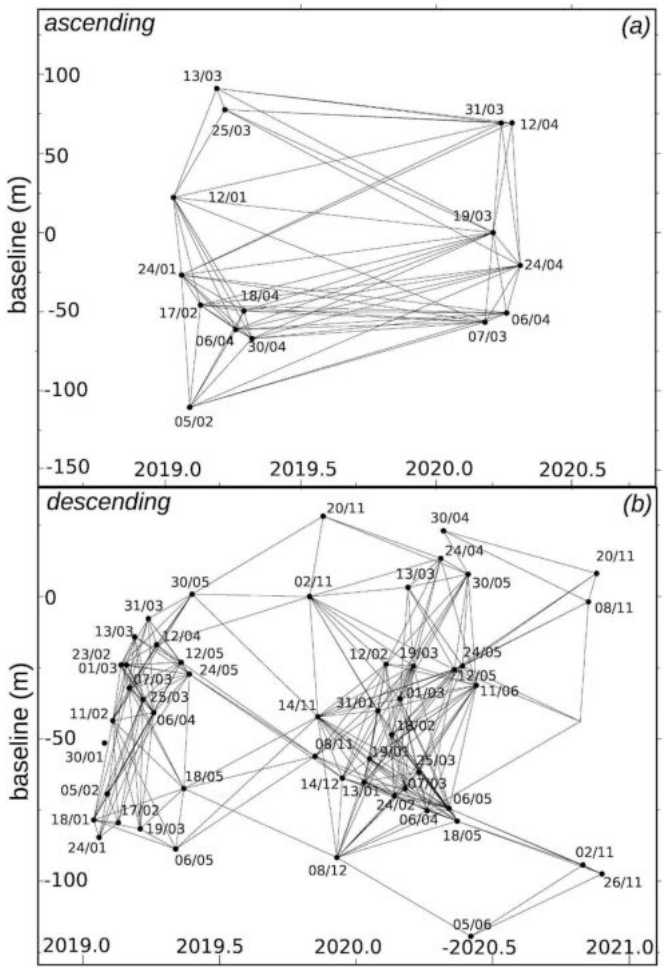

Fig. 2. Baselines versus date for the interferometric pairs. The interferometric pairs were selected considering a temporal and spatial baseline threshold of (a) 450 days and 100 m for the ascending configuration, and (b) 210 days and 50 m for the descending configuration. Each dot is labeled by the corresponding date (day/month).

satellite configuration (Fig. 4): from April 2019 to April 2020 for ascending orbits, from October 2019 to November 2020 for descending orbits.

2.3. Atmospheric noise and observed deformation

Atmospheric noise is seasonal, with the months of March, April, and May of 2019 and 2020 the most affected, and varies from few millimeters to 45 mm. We considered several factors when correcting this noise:

1. The common-point stacking approach has better performance if the dates of the scenes involved are continuous. This is not the case for both datasets, especially for the ascending data.
2. The assumption of this approach is that noise is randomly distributed in time. In this sense, the stratified tropospheric layer correlated to the volcano edifice and geometry may not always be random in a short time, therefore it could lead to a misinterpretation of atmospheric noise as slow deformation. After the atmospheric correction was applied, we observed a smoother deformation in both satellite configurations, without modifying the general deformation pattern and with no significant change in the final cumulative displacement. However, this does not imply the absence of atmospheric noise residuals.
3. The standard deviation calculated in non-deformed areas at each scene after the atmospheric correction (bar error in displacement curve from Fig. 3), indicates larger noise in the descending data than on the ascending data, even though the descending dates are much denser than in the ascending case. This is consistent with the different values found in the cumulative displacement maps from ascending and descending (Fig. 4).

The complete set of APS, and the corrected and uncorrected scene maps, are available in Appendix A, Figs. A1-A6.

The red dashed line in Fig. 3 divides the time interval analyzed into two different periods: January–October 2019 and October 2019–November 2020. Because of the lack of SAR images for ascending orbits in the Sentinel-1 catalogue between May 2019 and March 2020, the ascending curve presents several discontinuities.

The first period of the time-series (January to May 2019) presents no major deformation, except for small fluctuations around zero at the end of this first period in the northeast flank where the active crater is located (pixel B and B*, Fig. 3c and d; see Fig. 4 for location of the pixels). Some small displacements could be related to local activity such as hydrothermal overpressure release but most of the observed deformation is residual from the correction of atmospheric noise.

The second period, from October 2019 to November 2020 (Fig. 3), shows a clear displacement towards the sensor's line-of-sight for both orbits (see Figs. 3 and 4, pixels A, A*, B, B*, C, and C*). According to Cardona et al. (2021), the GNSS stations registered an uplift from the end of July 2019. Unfortunately, the seasonal discontinuity in the time-series curves from the end of May to the end of October limits the observation of the beginning of the deformation. The time-series of descending orbits from October 2019 to June 2020 (Fig. 3a, c, and f) shows a smoothly increasing displacement towards the line-of-sight, reaching a maximum value of approximately 90 mm in November 2020. Because of the lack of SAR images for ascending orbits between May 2019 and March 2020, the time-series seems to present an abrupt increase from almost zero displacement to 80–120 mm (Fig. 3b, d, and f).

Fig. 4 shows the cumulative displacement per year for the ascending and descending orbits for the second period. A displacement towards the sensor's line-of-sight can be observed in both satellite orbits (ascending/descending), centered in the Las Termas volcanic subcomplex, the center of volcanic activity in the last century (Fig. 4a). Maximum observed deformation is approximately 100 mm/year for the descending orbit, and approximately 120 mm/year for ascending orbits. The differences between the ascending and descending values could be explained by either a large horizontal deformation component in the local deformation or residuals from the atmospheric correction (Fig. 3).

3. Modeling

3.1. Modeling approach

We performed a joint inversion of ascending and descending cumulative displacement per year from October 2019 to November 2020 (Fig. 4), using dMODELS (Battaglia et al., 2013). This software package implements analytical solutions for sources embedded in a homogeneous elastic half-space. This approach employs pressurized cavities of simple geometries to approximate the crustal stress field of the actual source. The inversion algorithm is a weighted least-squares algorithm combined with a random search grid to find the minimum of the penalty function, the chi-square per degree of freedom. Results are presented in Table 2.

The original dataset was down sampled up to 5% (or a constant step of 1 pixel every 20) to reduce the computational cost. Because of the low spatial gradient of the displacement (and the processing coherence threshold), there was no need to employ more complex algorithms (e.g., gradient-based methods such as Quadtree) in this case (Pritchard et al.,

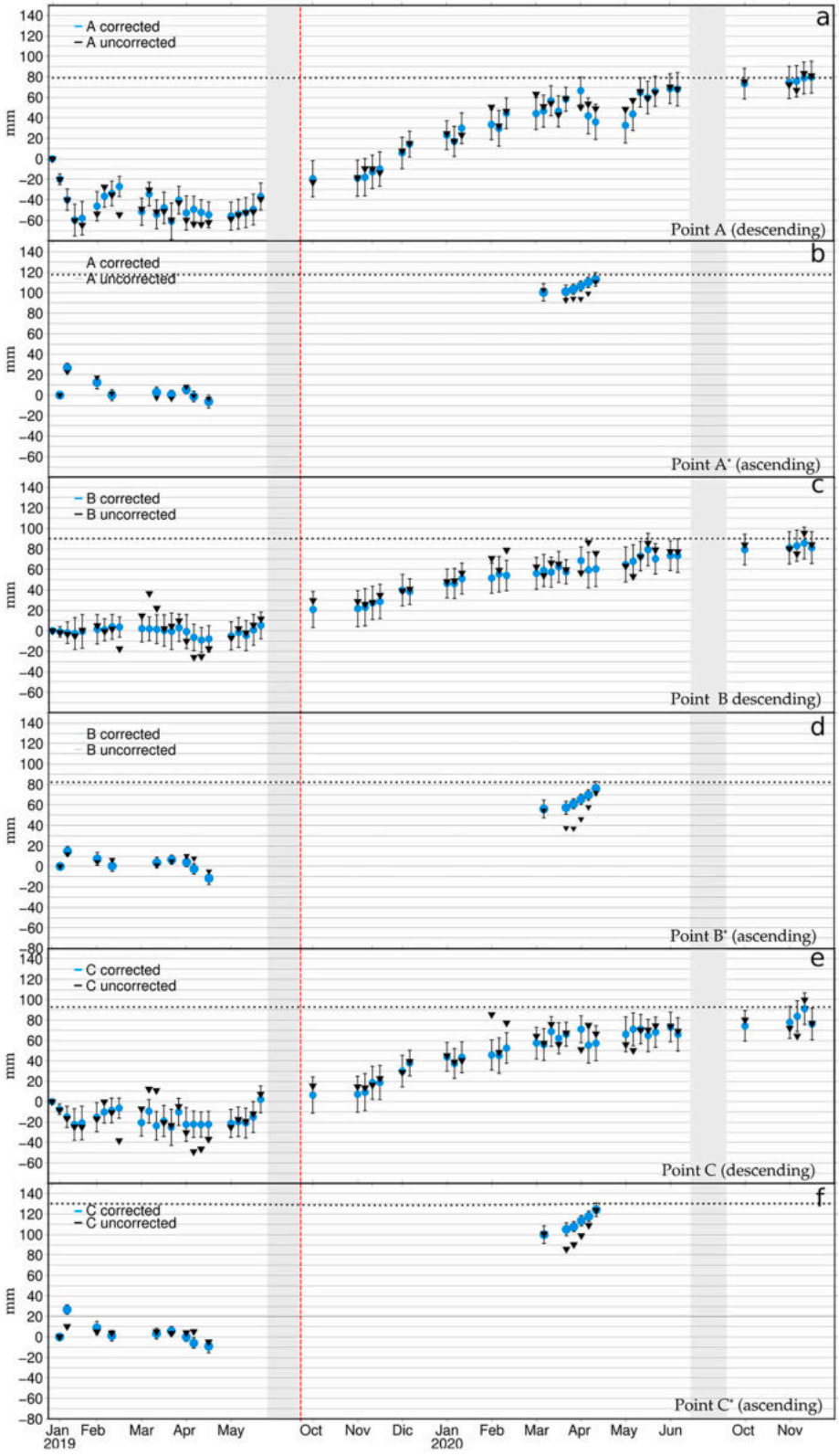

Fig. 3. Displacement time-series for descending (a, c, and, e) and ascending (b, d, and, f) configurations. A, A*, B, B*, C, and C* correspond to the points marked in Fig. 4. The dates taken as relative initial time for the SBAS time-series are January 6, 2019, for descending orbits and January 12, 2019, for ascending orbits. The black triangles correspond to data without the atmospheric correction, while the light blue dots correspond to data after the atmospheric correction. The error bars for each data point represent the standard deviation of a non-deforming area for each date. The red line indicates the period in which DInSAR signal presents a clear deformation towards the line-of-sight. The dotted black lines indicate the maximum values of deformation. The gray rectangles correspond to the winter months from 2019 and 2020 when no information could be extracted from the interferograms because of the presence of snow; see text for more details. (For interpretation of the references to colour in this figure legend, the reader is referred to the web version of this article.)

2002).

The quantitative analysis to determine the best fit model is based on two statistical indices (see Table 2): the value of the penalty function χ^2_ν, and the root mean square error (RMSE) of the comparison between the semivariograms of models and dataset. The semivariogram provides a measure of the spatial distribution of the DInSAR dataset and results from the different models and allows a quantitative evaluation of the ability of the model to mimic the spatial distribution of the data (e.g., Battaglia et al., 2021). Finally, model results were also compared with the available geological/geophysical data to verify that the best-fit source is appropriate for the geological context of the studied area.

Errors for the best-fit parameters are estimated using a Monte Carlo

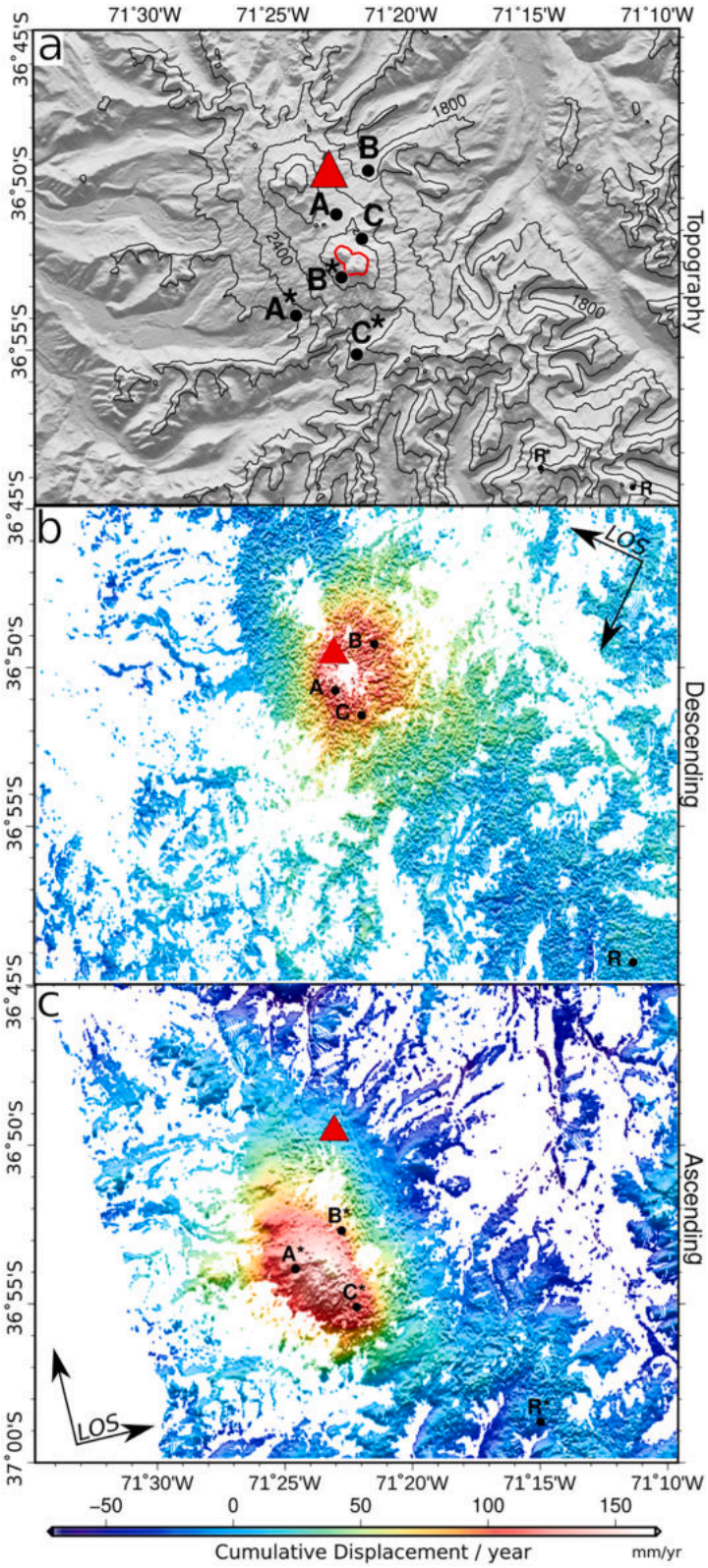

Fig. 4. Cumulative displacements per year of SBAS time-series from October 2019 to November 2020 for descending orbits, and from April 2019 to April 2020 for the ascending orbits. The motion towards the sensor's line-of-sight direction represents inflation. (a) Digital elevation model SRTM (90 m) of the volcanic complex of Nevados de Chillán, the red contour corresponds to the active crater placed in the Las Termas subcomplex. (b) Cumulative displacements per year for descending orbits, superimposed to shaded topography. (c) Cumulative displacements per year for ascending orbits, superimposed to shaded topography. The points A, A*, B, B*, C, and C* correspond to the displacement versus time curves in Fig. 3. R and R* correspond to a stable area taken as reference for calculating the relative deformation. (For interpretation of the references to colour in this figure legend, the reader is referred to the web version of this article.)

simulation technique (Wright et al., 2001): white noise is added to the original dataset and the noisy dataset is then inverted to determine the best-fit parameters. This process is repeated 100 times to create a distribution of values for each best fit parameter. The standard deviation of this distribution is assumed to be a good estimate of the uncertainty of the best fit parameter (Table 2).

3.2. Modeling results

Results from the joint inversion of cumulative displacement per year from ascending and descending orbits are presented in Table 2. The best fit solution for radially symmetric sources (sphere, spheroid, and sill) infers an intrusion located beneath Nevados de Chillán, 5 to 8 km below

Table 2
Parameters of best-fit sources. All depths are relative to the crater. Okada's parameters correspond to the initial (top) and final (bottom) location of the dike. A smaller RMSE (the variogram's root-mean-square error) indicates that the source better reproduces the data spatial distribution.

Source	χ^2_ν	Lat (°)	Long (°)	Depth (km)	Radius (m)	δV $\times 10^6$ m^3/yr	RMSE
Sphere	6.2	−36.89	−71.39	6.2	1000	18	0.071
Spheroid	5.4	−36.89 ± 0.04	−71.38 ± 0.05	5.5 ± 0.5	850	22 ± 7	0.051
Sill	7.6	−36.87	−71.39	8.3	657	19	0.121
Opening dike	4.1	−36.84 ± 0.03 −36.89 ± 0.04	−71.42 ± 0.03 −71.32 ± 0.04	1 ± 0.2 6.5 ± 0.5	dip 77° ± 10° E Opening 0.4 ± 0.01 m	20 ± 11	0.105

the surface. Source locations are clustered on the west side of the Las Termas subcomplex, where the latest lava flows are located (Fig. 1). The best fit solution for an opening dike extends for 10 km on both subcomplexes of Nevados de Chillán with a strike of 305°.

We compare the two best-fit models, the opening dike and spheroid (see Table 2), in Figs. 5 and 6. The deformation field is centered in the Las Termas subcomplex, even though it appears skewed in the opposite directions because of the SAR line-of-sight.

Although the opening dike (Okada, 1985), dipping 77°E, has a smaller χ^2_ν error (Table 2), it presents a steep gradient opposite to the sensor's line-of-sight that is absent in the data (Fig. 6). The linear features in the residual panels (Fig. 5) and the asymmetric deformation shapes (Fig. 6) are modeling artifacts of the opening dike best fit solution, not observed in the deformation data. Our preferred model is the prolate spheroid, since its smaller root mean square error (RMSE) indicates that it better reproduces the data spatial distribution (Fig. 6, Fig. C1 in Appendix C).

It is worth noting that several factors can prevent a better fit:

1. The high values of noise present in the descending data, discussed in Section 2.3.
2. The possibility of having additional deformation from minor structures, such as the subvertical dikes proposed by Cardona et al. (2021), which interact with the deep magmatic reservoir and the shallow hydrothermal system.
3. Mechanical and structural discontinuities neglected by the models we employ.

A 3D representation of the prolate spheroid, placed in perspective with the topography of the volcanic complex of Nevados de Chillán, is shown in Fig. 7. The modeled geometry's semi-major axis aligns with the cones and craters trend, which is interpreted as the trace of the Chillán-Cortadera fault (see also Fig. 1). Seismic hypocenters (OVDAS report, 2021, *https://www.sernageomin.cl/complejo-volcanico-nevados-de-Chillán/*) cluster above the location of the spheroid.

4. Discussion

This work presents DInSAR time-series of surface deformation from the Sentinel-1 data at the volcanic complex of Nevados de Chillán from January 2019 to November 2020. Eruptions started in June 2016 and an uplift period was recorded by GNSS stations from August of 2019 (Cardona et al., 2021). This uplift is observed in the DInSAR time-series from October 2019 to November 2020. Sentinel-1 scenes from the months before October 2019 cannot be considered due to strong decorrelation for the presence of snow in the volcano edifice.

Even though intermittent columns of ash, gas, and pyroclastic material have been observed throughout 2019 and 2020, these became more frequent and energetic during the last months of 2020. These ash emissions (Fig. 8), together with the new lava flows observed in 2019,

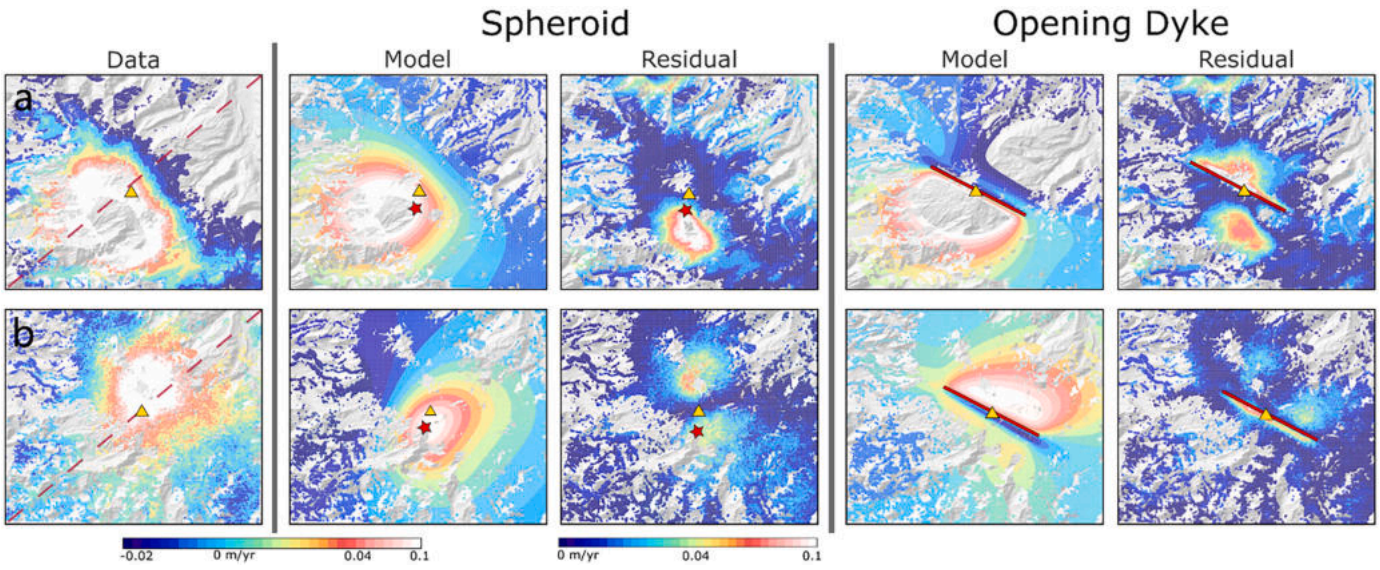

Fig. 5. Modeling results for opening dike and spheroid. (Top row) ascending orbit; (Bottom row) descending orbit. The yellow triangle is the current active vent of Nevados de Chillán, the red star is the location of the center of the best fit spheroid (spheroid panels) and the solid red line is the trace of best fit opening dike (opening dike panels). The dashed red lines (left column, data panels) identify the deformation profiles shown in Fig. 6. The linear features evident in the modeled and residual panels of the opening dike model are not observed in the dataset (Fig. 6). (For interpretation of the references to colour in this figure legend, the reader is referred to the web version of this article.)

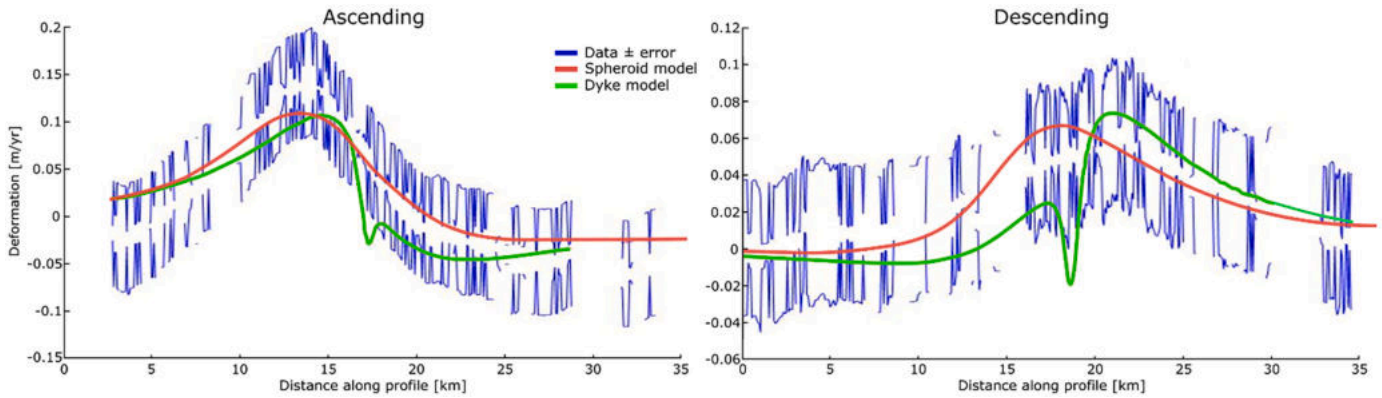

Fig. 6. Deformation profiles for ascending and descending orbits. The blue lines are the DInSAR data ± error, the red line is the spheroid model, and the green line is the opening dike model. The spheroid better reproduces the overall pattern of the deformation but underestimates the maximum deformation. The opening dike profile has a dip that is not present in the data. (For interpretation of the references to colour in this figure legend, the reader is referred to the web version of this article.)

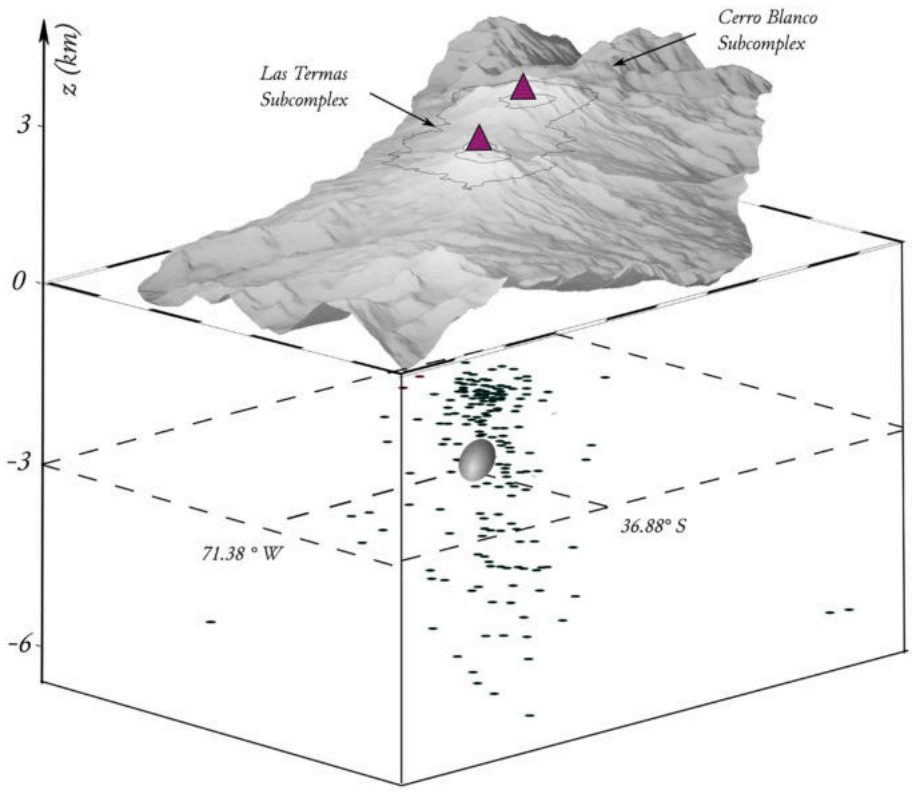

Fig. 7. Three-dimensional representation of the best-fit spheroid model, superimposed on a digital elevation model (SRTM 3-arc sec) of the volcanic complex of Nevados de Chillán. Black dots correspond to hypocenters of seismic events reported by OVDAS for the period January 2019–November 2020 (OVDAS report, 2021). The modeled geometry orientation coincides with the volcanic cones and craters trend, while hypocenters cluster over the top of the deformation source.

suggest a continuous intrusion in the reservoir feeding the eruptive cycle coupled with intermittent release of material.

The period from October 2019 to November 2020 was characterized by a significant displacement towards the sensor's line-of-sight (LOS) of approximately 100 mm in both orbits. According to OVDAS, incandescent material was observed from the active crater in the Las Termas subcomplex in January 2019. This material resulted from an explosion that partially destroyed a dome observed inside the active crater in early 2018. From January 2019 to September 2019, the volcanic complex experienced several long-period seismic events with explosions of ash, pyroclastic material, and gases columns less than 1 km high. In October 2019, a new emission point was detected in the active crater, and low amplitude volcano-tectonic seismic events (magnitude $M_L \sim 3$) became frequent. In mid-2020, ash columns approximately 2–3 km high were also observed (OVDAS report, 2021).

We observe a strong correspondence between the volcanic activity described above and the LOS displacements (Figs. 3, 4, and 9). The first period of the time-series, January to October 2019, started with the explosion in January that destroyed the dome inside the active crater (Fig. 3). The decrease in seismic activity, explosive events, and dome growth rate between January 2018 to August 2019 (Moussallam et al., 2021) correlates with this first time-series period of no significant deformation (pixel B and B*, Fig. 3c and d).

For the second period, October 2019 to November 2020, the

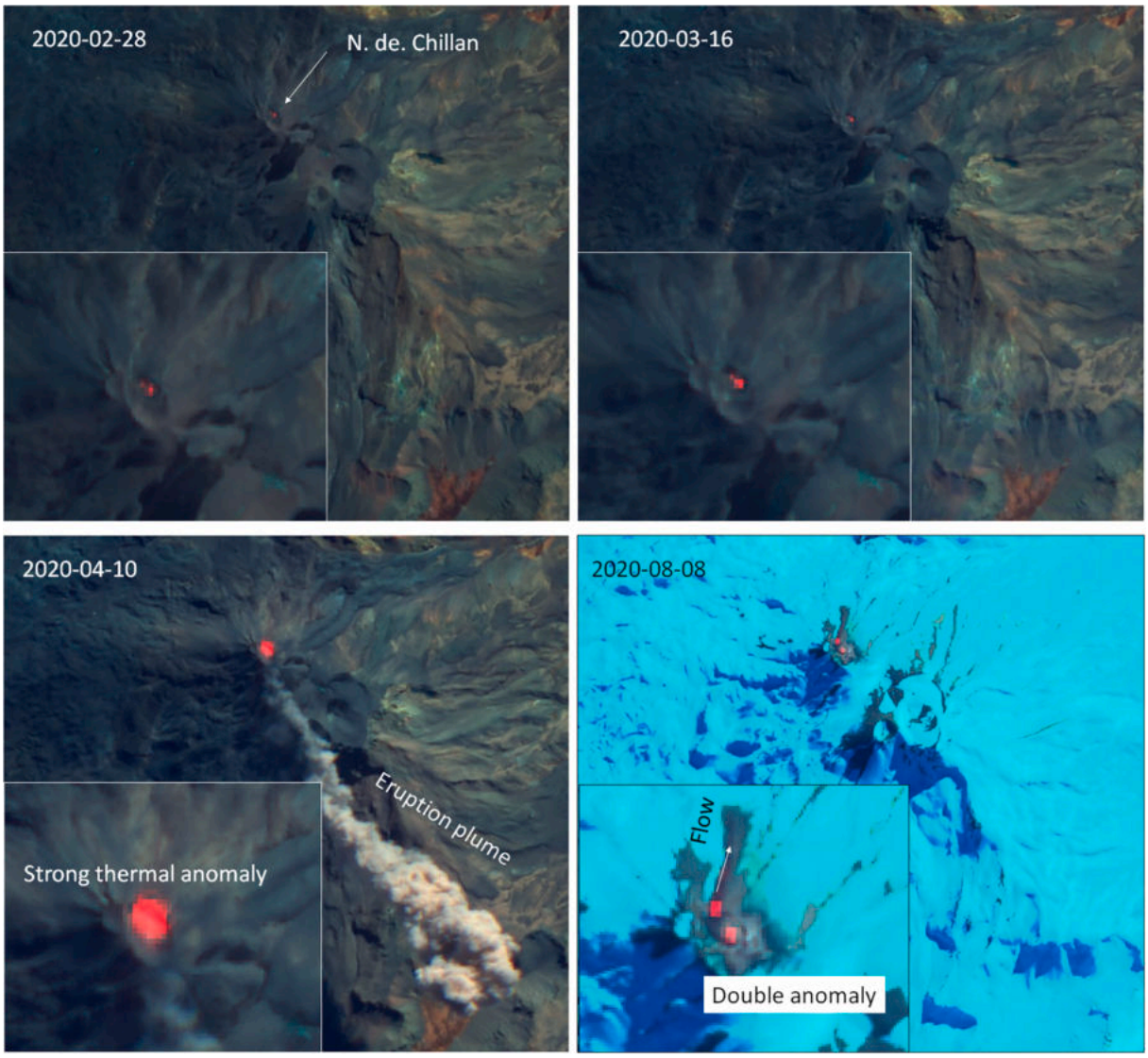

Fig. 8. Satellite images from Sentinel-2 evidence a strong thermal anomaly at the Las Termas subcomplex during the deformation period observed in the DInSAR time-series from Sentinel-1 data. Ash and pyroclastic columns can be observed in the third panel (April 10, 2020). A double thermal anomaly is observed in the August 2020 panel.

displacement towards the LOS (about 100 mm; Figs. 3 and 4) correlates with the long-period seismic events followed by more frequent volcano-tectonic activity at approximately 4 km depth. This seismic activity and the displacement towards the sensor's line-of-sight can be associated with a new injection of magma that increases the pressure and triggers volcano-tectonic events and the extrusion of lava flows, Fig. 9.

The prolate spheroid source (Table 2) better reproduces the overall deformation pattern (Fig. 6). This source aligns with the northwest to southeast trend of the Chillán-Cortadera fault, and its depth (5.5 ± 0.5 km below the surface) is closely related to the location and hypocenters of LPs and seismic tremor (Fig. 7). The volcanic complex of Nevados de Chillán source depth is comparable with that inferred for nearby volcanoes under similar tectonics stresses, Laguna del Maule (~5 km depth, Singer et al., 2014; Feigl et al., 2014) and Domuyo (4–7 km; Astort et al., 2019). The prolate spheroid source probably coexists with a subvertical dike system (Cardona et al., 2021), connecting it to the surface. According to Lundgren et al. (2017), Copahue possesses a similar feeding reservoir (a shallow elongated source), connected to the surface of the caldera by a plunging dike.

Finally, Moussallam et al. (2018) proposed three possible future scenarios for this unrest episode: (I) a gradual end of unrest without extrusions; (II) transition to a magmatic eruption with explosive activity and pyroclastic flows; (III) persistent low activity, frequent outgassing, and eventual transition to scenarios I or II. The results presented in this study suggest that activity at Nevados de Chillán has been evolving towards the third scenario. The depressurization processes described by Moussallam et al. (2021) are probably preventing a large accumulation of volatiles and pressure changes needed to have explosive eruptions of higher energy.

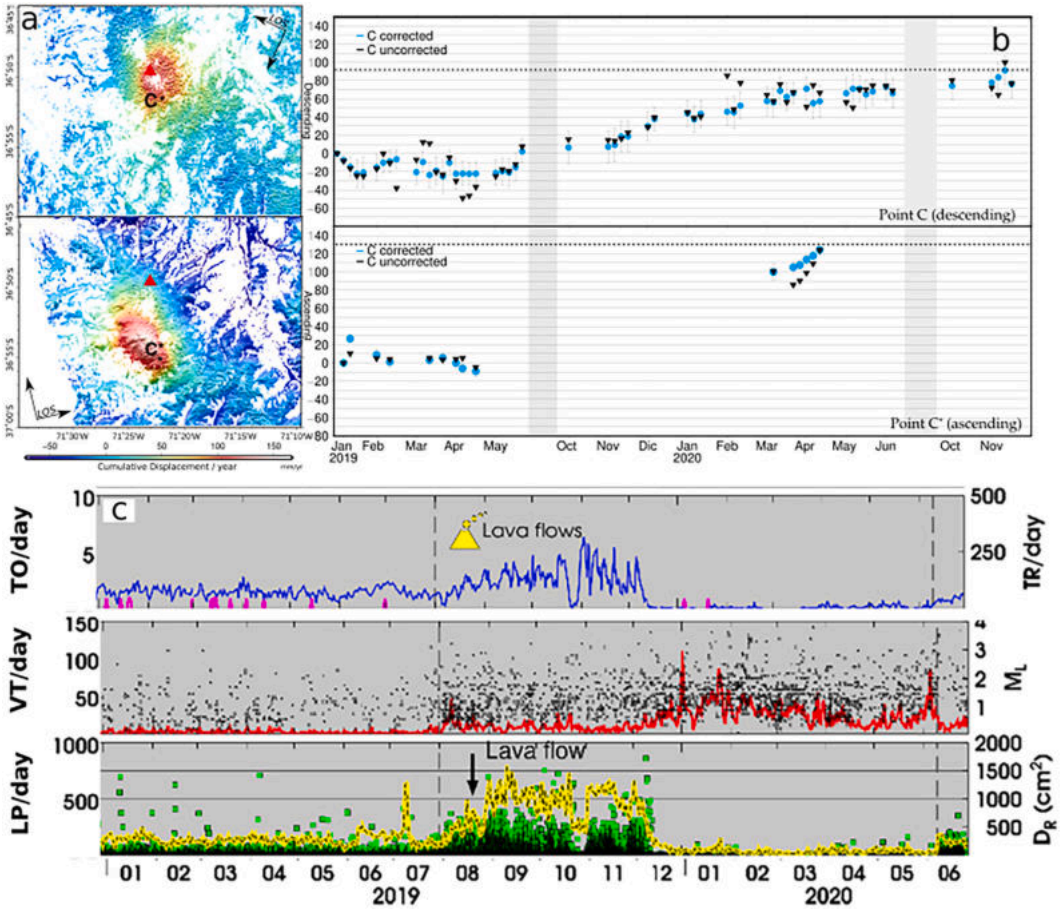

Fig. 9. Correlation between DInSAR time-series and seismic activity reported by Cardona et al. (2021). a) Maps of cumulative displacements per year at pixels C and C* near the active crater; (b) SBAS time-series from October 2019 to November 2020 at C and C*; c) Seismicity and lava flows from the volcanic complex of Nevados de Chillán (modified after Cardona et al., 2021); TR/day panel - magenta line: daily tornillo-type; blue line: daily seismic tremor; ML panel – red line: daily volcano-tectonic (red line); black dots: local magnitude; DR panel- yellow line: daily long-period; green line: reduced displacement calculated from the LP seismic activity. The increase in seismic activity from August 2019 correlates with the displacements towards the sensor's line-of-sight. Four lava flows were observed at the active crater in August 2019. (For interpretation of the references to colour in this figure legend, the reader is referred to the web version of this article.)

Data

Sentinel-1 data were freely provided by the ESA Copernicus Programme. All information about seismicity was extracted from the reports available online at https://www.sernageomin.cl/complejo-volcanico-nevados-de-Chillán/. Each report includes a description of ash emissions, and location, depth and type of seismic activity recorded. The open-source processing tools employed in this work, Generic Mapping Tools (GMT) and GMTSAR, were provided by Wessel et al. (1998) and Sandwell et al. (2011a, 2011b). dMODELS is an open-source software developed by the USGS Volcano Disaster Assistance Program (https://pubs.er.usgs.gov/publication/tm13B1). The latest version of dMODELS is available from M. Battaglia (mbattaglia@usgs.gov).

CRediT authorship contribution statement

Ana Astort: Conceptualization, Methodology, Writing – original draft. **Gregorio Boixart:** Conceptualization, Methodology, Writing – original draft. **Andrés Folguera:** Review and editing. **Maurizio Battaglia:** Writing – review & editing, Software.

Declaration of Competing Interest

The authors declare that they have no known competing financial interests or personal relationships that could have appeared to influence the work reported in this paper.

Acknowledgments

Comments and suggestions by Francisco Delgado (Universidad de Chile), one anonymous reviewer, Stephanie Prejean (USGS), Leonardo D. Euillades (Universidad Nacional de Cuyo) and Pablo A. Euillades (Universidad Nacional de Cuyo) greatly helped to improve this study. Funding for this work came from UBA-CONICET, USAID via the Volcano Disaster Assistance Program and from the U.S. Geological Survey (USGS) Volcano Hazards Program. Any use of trade, firm, or product names is for descriptive purposes only and does not imply endorsement by the U.S. Government.

Appendix A. Line-of-sight deformation maps with and without atmospheric corrections

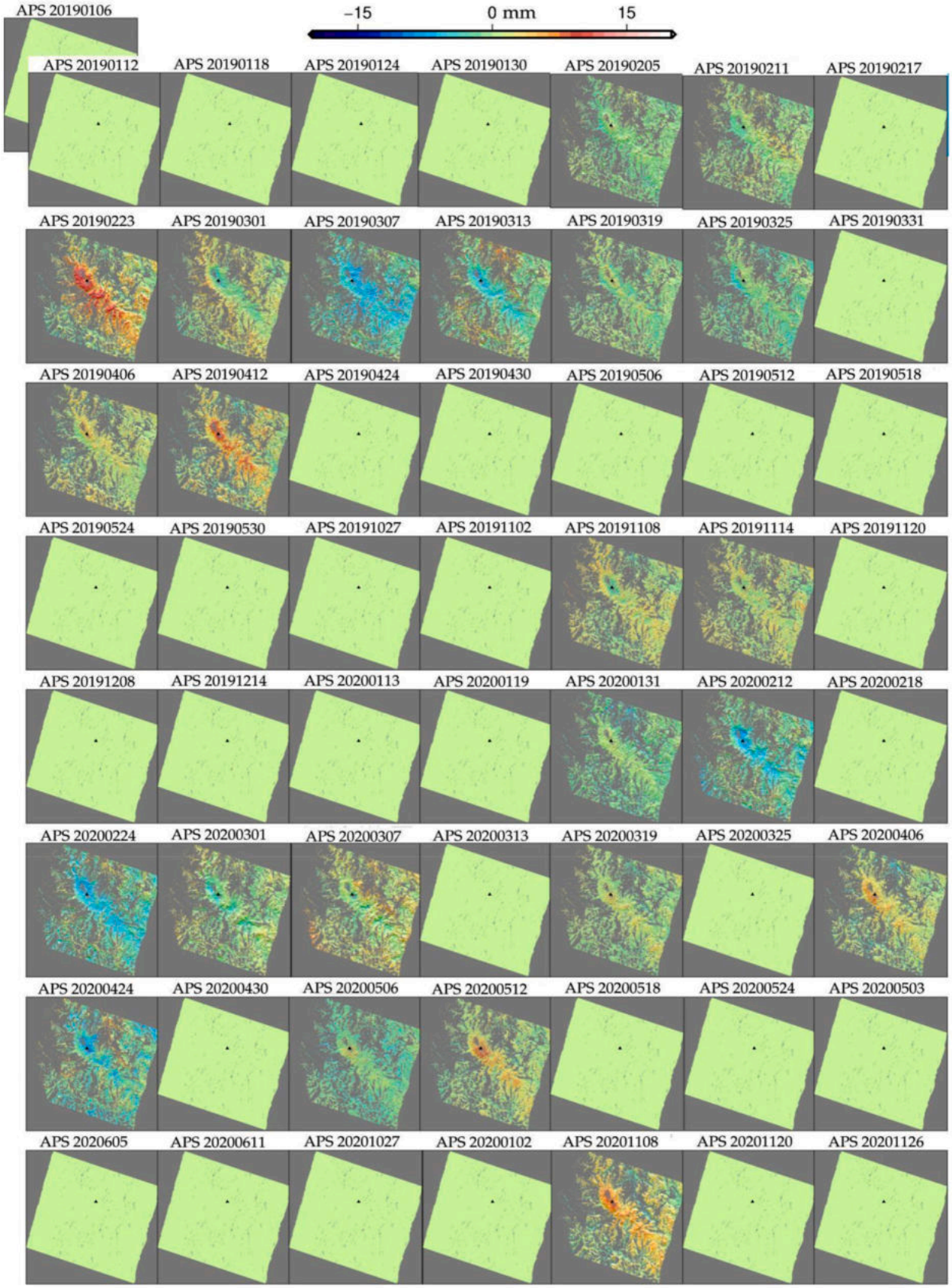

Fig. A1. Descending orbits. Atmospheric noise for each scene, estimated from stacking of common points between nearby date grids.

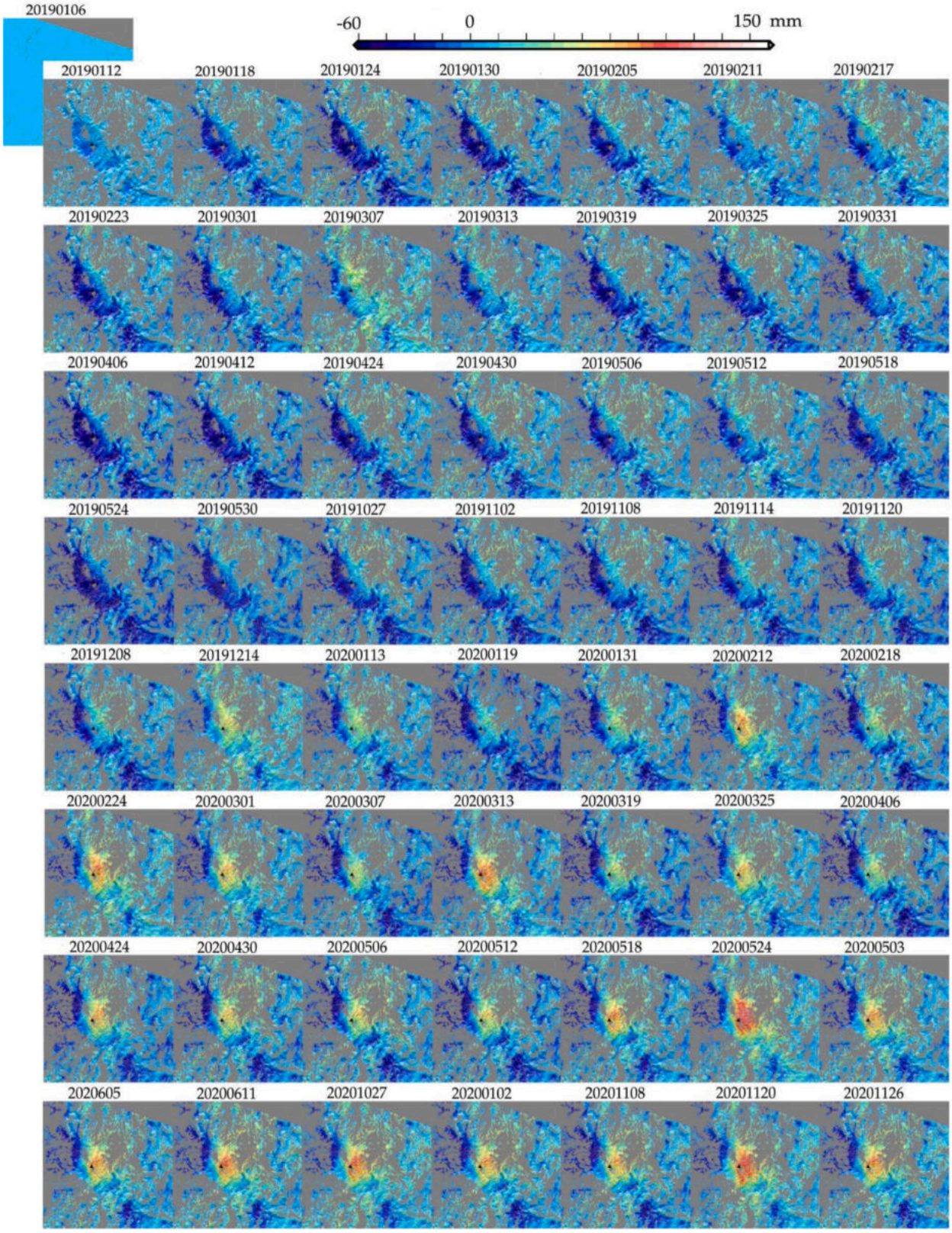

Fig. A2. Descending orbits. Displacement without atmospheric correction applied.

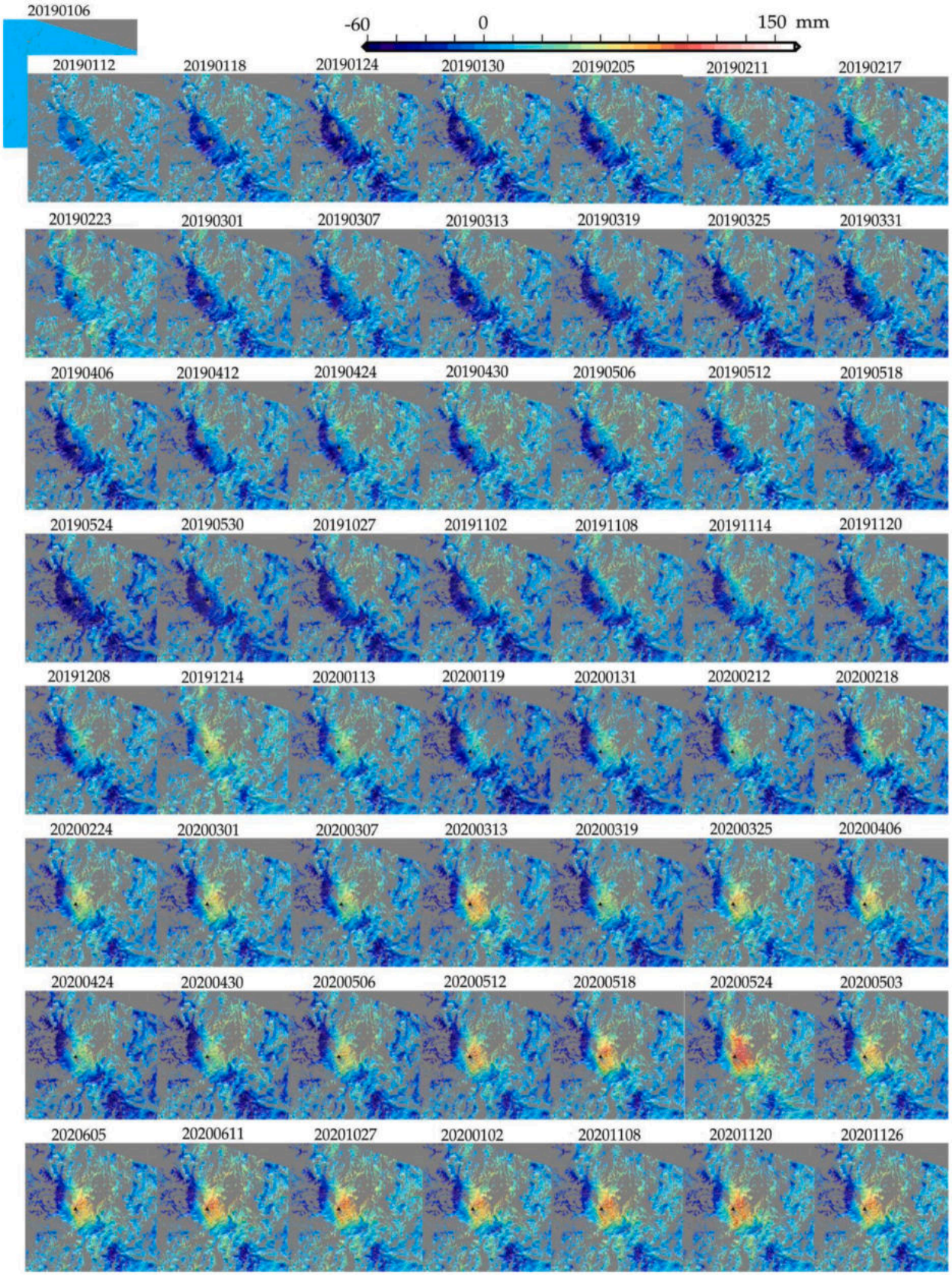

Fig. A3. Descending orbits. Displacement with atmospheric correction applied for each scene, estimated from stacking of common points between nearby date grids.

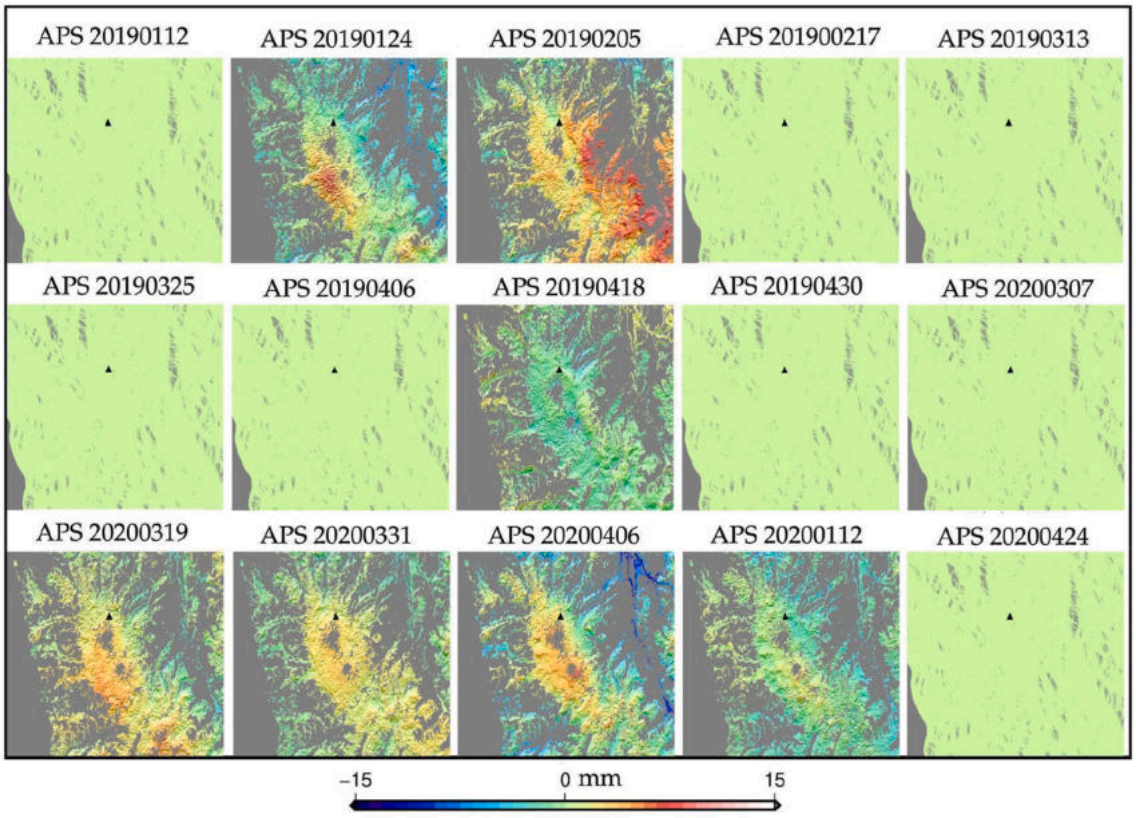

Fig. A4. Ascending orbits. Atmospheric noise estimated from stacking of common points between nearby date grids.

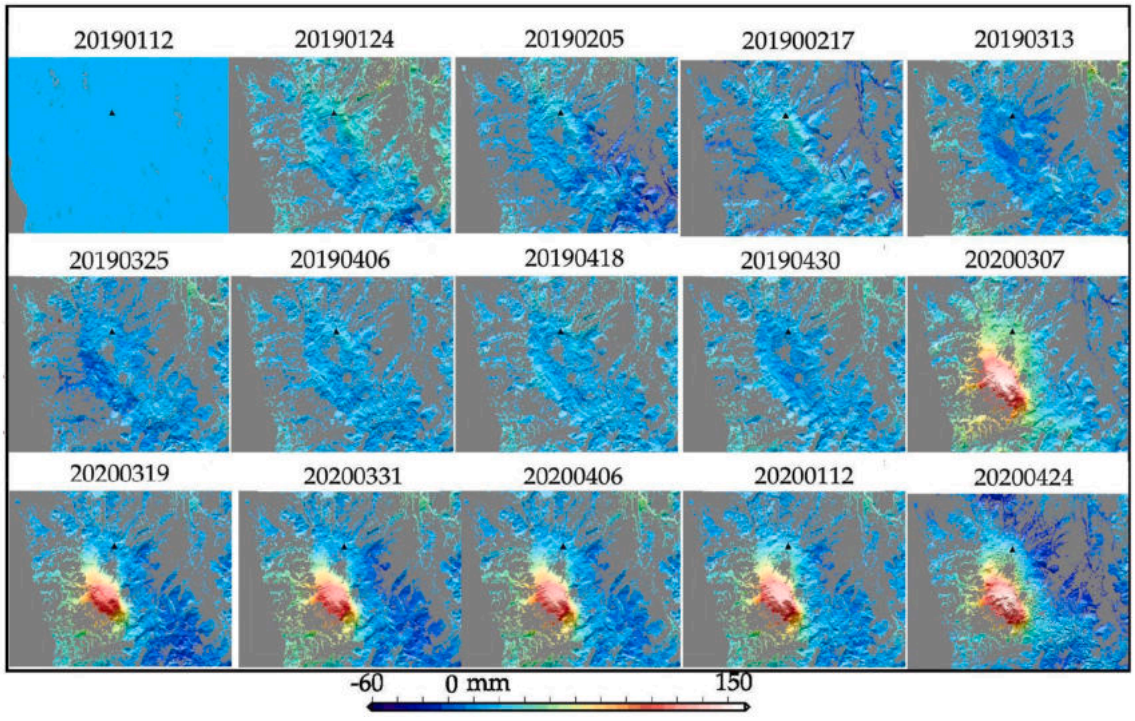

Fig. A5. Ascending orbits. Displacement without atmospheric correction applied.

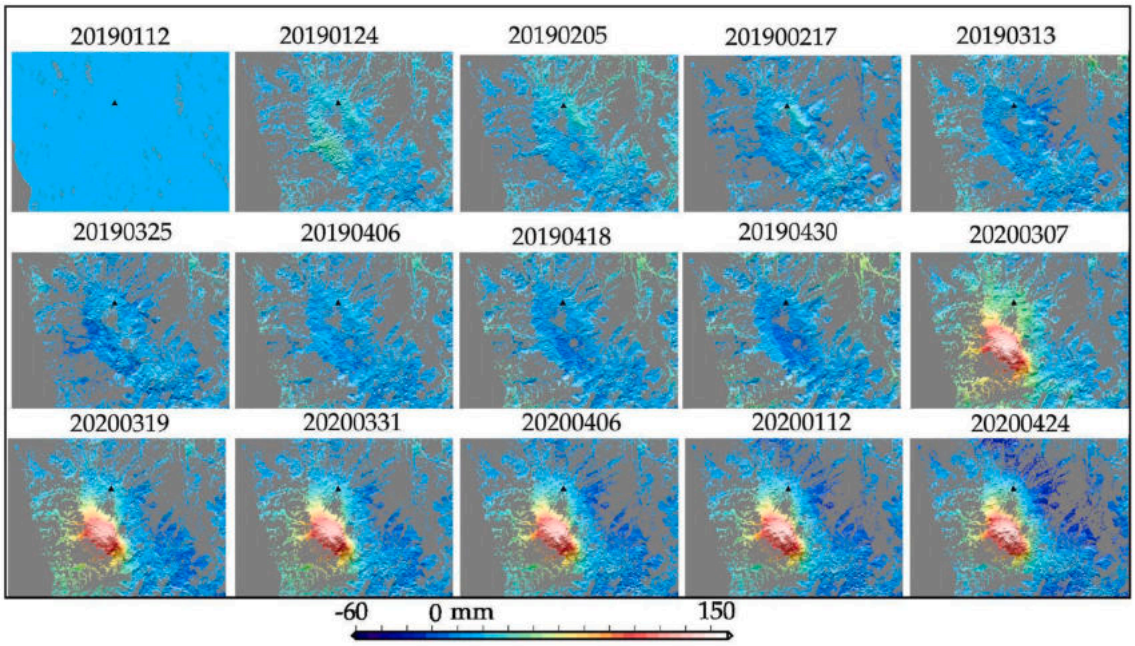

Fig. A6. Ascending orbits. Displacement with atmospheric correction applied.

Appendix B. Data tables

Table B1
Interferometric pairs for the descending configuration Sentinel-1.

Master	Slave	B_{perp}[m]	Master	Slave	B_{perp}[m]	Master	Slave	B_{perp}[m]	Master	Slave	B_{perp}[m]
20190518	20191114	−30.57	20200113	20200325	−0.00	20191208	20200307	−24.06	20200307	20200319	−45.78
20190518	20191208	20.49	20200113	20200406	16.15	20191208	20200325	−29.87	20200307	20200506	12.40
20190524	20191108	27.21	20200113	20200506	18.20	20191208	20200406	−13.71	20200307	20200518	17.17
20190524	20191214	33.22	20200113	20200512	−33.19	20191208	20200506	−11.66	20200313	20200319	29.77
20190530	20191102	−5.04	20200113	20200524	−33.97	20191208	20200518	−6.89	20200313	20200424	-3.82
20190530	20191114	40.46	20200119	20200131	−16.89	20191214	20200107	47.08	20200313	20200512	36.56
20190530	20191120	−37.09	20200119	20200212	−35.03	20191214	20200131	−23.90	20200313	20200524	35.78
20191102	20191114	45.51	20200119	20200307	13.53	20191214	20200212	−42.04	20200319	20200424	−33.60
20191102	20191120	−32.05	20200119	20200319	−32.24	20191214	20200224	8.19	20200319	20200506	58.18
20191102	20200131	42.08	20200119	20200506	25.94	20191214	20200319	−39.25	20200325	20200406	16.15
20191102	20200212	23.94	20200119	20200518	30.71	20191214	20200506	18.93	20200325	20200506	18.21
20191102	20200218	51.15	20200131	20200212	−18.14	20191214	20200518	23.70	20200325	20200512	−33.19
20191102	20200301	38.80	20200131	20200307	30.43	20200107	20200224	−38.89	20200325	20200518	22.98
20191102	20200313	−3.04	20200131	20200319	−15.34	20200107	20200307	−40.55	20200325	20200524	−33.97
20191102	20200319	26.73	20200131	20200506	42.83	20200107	20200506	−28.15	20200406	20200506	2.05
20191102	20200424	−6.87	20200131	20200518	47.60	20200107	20200518	−23.38	20200406	20200512	−49.34
20191102	20200512	33.52	20200212	20200224	50.23	20200113	20200119	−7.73	20200406	20200518	6.82
20191108	20191214	6.01	20200212	20200307	48.57	20200113	20200131	−24.63	20200506	20200518	4.77
20191108	20200131	−17.88	20200212	20200319	2.79	20200113	20200212	−42.77	20200512	20200524	−0.78
20191108	20200212	−36.02	20200212	20200424	−30.81	20200113	20200224	7.46	20191120	20200530	38.84
20191108	20200224	14.20	20200218	20200224	23.02	20200113	20200301	−27.90	20191208	20200605	−26.37
20191108	20200319	−33.23	20200218	20200301	−12.34	20200113	20200307	5.80	20191214	20200611	22.35
20191108	20200506	24.94	20190518	20191114	−30.57	20200113	20200325	−0.00	20200113	20200611	−27.10
20191114	20191208	51.06	20190518	20191208	20.49	20200113	20200406	16.15	20200119	20200611	−19.36
20191114	20191214	20.47	20190524	20191108	27.21	20200113	20200506	18.20	20200131	20200530	−45.38
20191114	20200113	21.20	20190524	20191214	33.22	20200113	20200512	−33.19	20200131	20200611	−2.46
20191114	20200131	−3.43	20190530	20191102	−5.04	20200113	20200524	−33.97	20200212	20200530	−27.24
20191114	20200212	−21.57	20190530	20191114	40.46	20200119	20200131	−16.89	20200212	20200611	15.67
20191114	20200224	28.66	20190530	20191120	−37.09	20200119	20200212	−35.03	20200218	20200611	−11.53
20191114	20200301	−6.70	20191102	20191114	45.51	20200119	20200307	13.53	20200224	20200611	−34.56
20191114	20200307	27.00	20191102	20191120	−32.05	20200119	20200319	−32.24	20200301	20200530	−42.11
20191114	20200319	−18.77	20191102	20200131	42.08	20200119	20200506	25.94	20200301	20200611	0.80
20191114	20200325	21.19	20191102	20200212	23.94	20200119	20200518	30.71	20200307	20200611	−32.90
20191114	20200406	37.35	20191102	20200218	51.15	20200131	20200212	−18.14	20200313	20200530	−0.25
20191114	20200506	39.40	20191102	20200301	38.80	20200131	20200307	30.43	20200313	20200611	42.65
20191114	20200512	−11.99	20191102	20200313	−3.04	20200131	20200319	−15.34	20200319	20200530	−30.03
20191114	20200524	−12.77	20191102	20200319	26.73	20200131	20200506	42.83	20200319	20200611	12.87
20191120	20200424	25.17	20191102	20200424	−6.87	20200131	20200518	47.60	20200325	20200611	−27.09
20191208	20191214	−30.59	20191102	20200512	33.52	20200212	20200224	50.23	20200406	20200611	−43.25

(*continued on next page*)

Table B1 (*continued*)

Master	Slave	B_{perp}[m]	Master	Slave	B_{perp}[m]	Master	Slave	B_{perp}[m]	Master	Slave	B_{perp}[m]
20191208	20200107	16.49	20191108	20191214	6.01	20200212	20200307	48.57	20200406	20201027	−35.95
20191208	20200113	−29.86	20191108	20200131	−17.88	20200212	20200319	2.79	20200424	20200530	3.56
20191208	20200119	−37.60	20191108	20200212	−36.02	20200212	20200424	−30.81	20200424	20200611	46.48
20191208	20200218	−45.42	20191108	20200224	14.20	20200218	20200224	23.02	20200430	20200530	16.27
20191208	20200224	−22.40	20191108	20200319	−33.23	20200218	20200301	−12.34	20200430	20201108	20.32
20191208	20200307	−24.06	20191108	20200506	24.94	20200218	20200307	21.36	20200430	20201120	9.33
20191208	20200325	−29.87	20191114	20191208	51.06	20200218	20200319	−24.41	20200506	20200611	−45.30
20191208	20200406	−13.71	20191114	20191214	20.47	20200218	20200325	15.55	20200506	20201102	16.25
20191208	20200506	−11.66	20191114	20200113	21.20	20200218	20200406	31.71	20200506	20201126	17.92
20191208	20200518	−6.89	20191114	20200131	−3.43	20200218	20200506	33.76	20200512	20200530	−36.82
20191214	20200107	47.08	20191114	20200212	−21.57	20200218	20200512	−17.63	20200512	20200611	6.09
20191214	20200131	−23.90	20191114	20200224	28.66	20200218	20200518	38.53	20200512	20201027	13.39
20191214	20200212	−42.04	20191114	20200301	−6.70	20200218	20200524	−18.41	20200512	20201108	−32.76
20191214	20200224	8.19	20191114	20200307	27.00	20200224	20200307	−1.66	20200512	20201120	−43.76
20191214	20200319	−39.25	20191114	20200319	−18.77	20200224	20200319	−47.44	20200518	20201102	11.48
20191214	20200506	18.93	20191114	20200325	21.19	20200224	20200506	10.74	20200518	20201126	13.15
20191214	20200518	23.70	20191114	20200406	37.35	20200224	20200518	15.51	20200524	20200530	−36.04
20200107	20200224	−38.89	20191114	20200506	39.40	20200301	20200307	33.70	20200524	20200611	6.87
20200107	20200307	−40.55	20191114	20200512	−11.99	20200301	20200313	−41.85	20200524	20201027	14.17
20200107	20200506	−28.15	20191114	20200524	−12.77	20200301	20200319	−12.07	20200524	20201108	−31.98
20200107	20200518	−23.38	20191120	20200424	25.17	20200301	20200325	27.90	20200524	20201120	−42.98
20200113	20200119	−7.73	20191208	20191214	−30.59	20200301	20200406	44.06	20200530	20200611	42.91
20200113	20200131	−24.63	20191208	20200107	16.49	20200301	20200424	−45.68	20200605	20201102	−34.25
20200113	20200212	−42.77	20191208	20200113	−29.86	20200301	20200506	46.11	20200605	20201126	−32.58
20200113	20200224	7.46	20191208	20200119	−37.60	20200301	20200512	−5.28	20201027	20201108	−46.16
20200113	20200301	−27.90	20191208	20200218	−45.42	20200301	20200518	50.88	20201102	20201126	1.66
20200113	20200307	5.80	20191208	20200224	−22.40	20200301	20200524	−6.07	20201108	20201120	−10.99

Table B2
Interferometric pairs for the ascending configuration Sentinel-1.

Master	Slave	B_{perp}[m]	Master	Slave	B_{perp}[m]
20190112	20190124	48.96	20190313	20190325	13.41
20190112	20190217	68.00	20190313	20200319	91.08
20190112	20190313	−68.88	20190313	20200331	21.82
20190112	20190325	−55.46	20190313	20200412	21.74
20190112	20190406	83.45	20190325	20200319	77.66
20190112	20190418	71.72	20190325	20200331	8.40
20190112	20190430	89.21	20190325	20200412	8.33
20190112	20200307	78.79	20190325	20200424	98.40
20190112	20200319	22.19	20190406	20190418	−11.73
2019011	20200331	−47.06	20190406	20190430	5.75
20190124	20190205	83.63	20190406	20200307	−4.66
20190124	20190217	19.04	20190406	20200319	−61.26
20190124	20190406	34.49	20190406	20200406	−10.49
20190124	20190418	22.76	20190406	20200424	−40.51
20190124	20190430	40.25	20190418	20190430	17.49
20190124	20200307	29.83	20190418	20200307	7.07
20190124	20200319	−26.76	20190418	20200319	−49.52
20190124	20200331	−96.02	20190418	20200406	1.23
20190124	20200406	24.00	20190418	20200424	−28.77
20190124	20200412	−96.09	20190430	20200307	−10.41
20190205	20190217	−64.59	20190430	20200319	−67.01
20190205	20190406	−49.14	20190430	20200406	−16.25
20190205	20190418	−60.87	20190430	20200424	−46.27
20190205	20190430	−43.38	20200307	20200319	−56.59
20190205	20200307	−53.80	20200307	20200406	-5.83
20190205	20200406	−59.63	20200307	20200424	−35.85
20190205	20200424	−89.65	20200319	20200331	−69.25
20190217	20190406	15.45	20200319	20200406	50.76
20190217	20190418	3.71	20200319	20200412	−69.33
20190217	20190430	21.20	20200319	20200424	20.74
20190217	20200307	10.79	20200331	20200412	-0.07
20190217	20200319	−45.80	20200331	20200424	90.00
20190217	20200406	4.95	20200406	20200424	−30.01
20190217	20200424	−25.06	20200412	20200424	90.07

Appendix C. Semivariograms

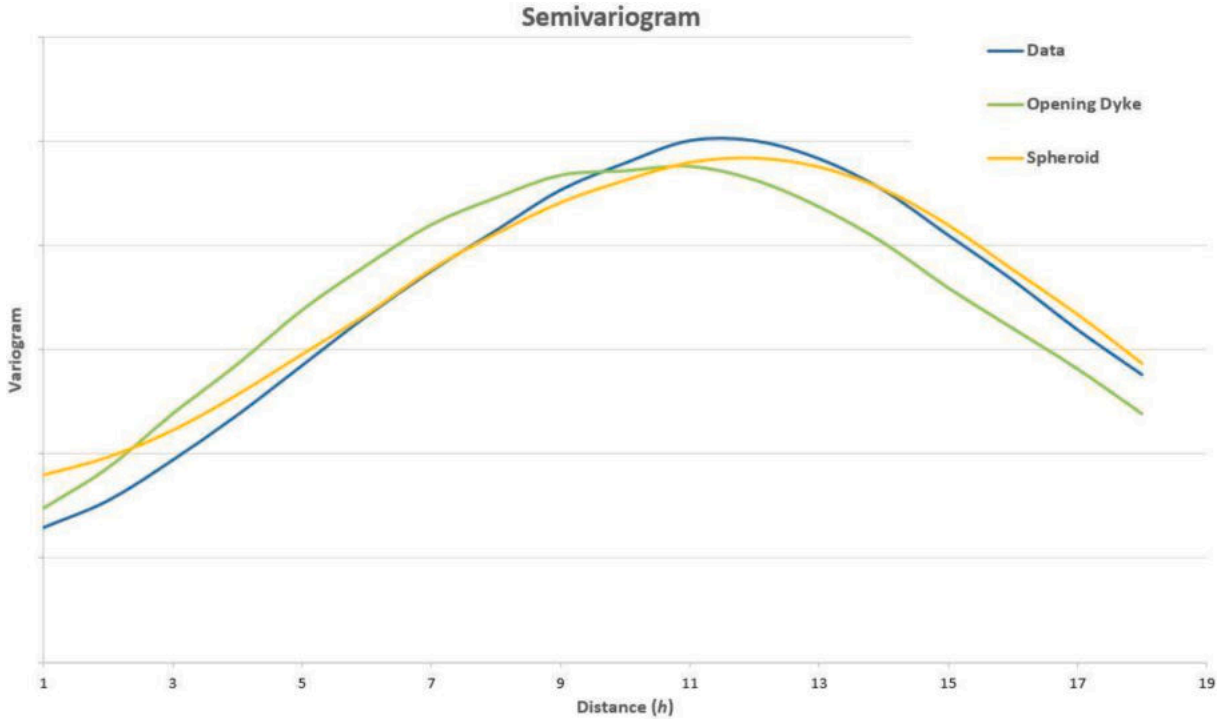

Fig. C1. Semivariograms of deformation (blue), opening dike model (green) and spheroid model (orange). Note the ability of the spheroid model (orange) to mimic the spatial distribution of deformation (blue) while the opening dike (green) variogram has a significant offset. (For interpretation of the references to colour in this figure legend, the reader is referred to the web version of this article.)

References

Astort, A., Walter, T.R., Ruiz, F., Sagripanti, L., Nacif, A., Acosta, G., Folguera, A., 2019. Unrest at Domuyo volcano, Argentina, detected by geophysical and geodetic data and morphometric analysis. Remote Sens. 11 (18), 2175. https://doi.org/10.3390/rs11182175.

Battaglia, M., Cervelli, P.F., Murray, J.R., 2013. dMODELS: a MATLAB software package for modeling crustal deformation near active faults and volcanic centers. J. Volcanol. Geotherm. Res. 254, 1–4. https://doi.org/10.1016/j.jvolgeores.2012.12.018.

Battaglia, M., Pagli, C., Meuti, S., 2021. The 2008–2010 Subsidence of Dallol Volcano on the Spreading Erta Ale Ridge: InSAR Observations and Source Models. Remote Sens. 13 (10), 1991. https://doi.org/10.3390/rs13101991.

Berardino, P., Fornaro, G., Lanari, R., Sansosti, E., 2002. A new algorithm for surface deformation monitoring based on small baseline differential SAR interferograms. IEEE Trans. Geosci. Remote Sens. 40 (11), 2375–2383. https://doi.org/10.1109/TGRS.2002.803792.

Cardona, C., Gil-Cruz, F., Franco-Marín, L., San Martín, J., Valderrama, O., Lazo, J., Bucarey, C., 2021. Volcanic activity accompanying the emplacement of dacitic lava domes and effusion of lava flows at Nevados de Chillán Volcanic Complex–Chilean Andes (2012 to 2020). J. Volcanol. Geotherm. Res. 107409 https://doi.org/10.1016/j.jvolgeores.2021.107409.

Cembrano, J., Lara, L., 2009. The link between volcanism and tectonics in the southern volcanic zone of the Chilean Andes: a review. Tectonophysics 471 (1–2), 96–113. https://doi.org/10.1016/j.tecto.2009.02.038.

Chen, C.W., Zebker, H.A., 2002. Phase Unwrapping for large SAR Interferograms: Statistical Segmentation and Generalized Network Models. IEEE Trans. Geosci. Remote Sens. 40, 1709–1719. https://doi.org/10.1109/TGRS.2002.802453.

Coppola, D., Laiolo, M., Lara, L.E., Cigolini, C., Orozco, G., 2016. The 2008 "silent" eruption of Nevados de Chillán (Chile) detected from space: Effusive rates and trends from the MIROVA system. J. Volcanol. Geotherm. Res. 327, 322–329. https://doi.org/10.1016/j.jvolgeores.2016.08.016.

Delgado, F., 2021. Rhyolitic volcano dynamics in the Southern Andes: Contributions from 17 years of InSAR observations at Cordón Caulle volcano from 2003 to 2020. J. S. Am. Earth Sci. 106, 102841 https://doi.org/10.1016/j.jsames.2020.102841.

Dixon, H., Murphy, M., Sparks, S., Chávez, R., Naranjo, J.A., Dunkley, P., Young, S., Gilbert, J., Pringle, M., 1999. The geology of Nevados de Chillán volcano, Chile. Rev. Geol. Chile 26, 227–253. https://doi.org/10.4067/S0716-02081999000200006.

Eggert, S., Walter, T.R., 2009. Volcanic activity before and after large tectonic earthquakes: observations and statistical significance. Tectonophysics 471 (1–2), 14–26. https://doi.org/10.1016/j.tecto.2008.10.003.

Elissondo, M., Baumann, V., Herrero, J.C., Gonzalez, R., Bonadonna, C., Biass, S., Bertagnini, A., 2015. Chronology and impact of the 2011 Puyehue-Cordón Caulle eruption, Chile. Nat. Hazards Earth Syst. Sci. Discuss. 3 (9) https://doi.org/10.5194/nhessd-3-5383-2015.

Farías, C., Basualto, D., 2020. Reactivating and calming volcanoes: the 2015 MW 8.3 Illapel megathrust strike. Geophys. Res. Lett. 47 (16), e2020GL087738 https://doi.org/10.1029/2020GL087738.

Farías, C., Galván, B., 2019. Numerical wave propagation study of the unusual response of Nevados de Chillán volcano to two aftershocks of the 2010 M_W=8.8 Maule earthquake. J. Volcanol. Geotherm. Res. 389, 106735 https://doi.org/10.1016/j.jvolgeores.2019.106735.

Farías, C., Lupi, M., Fuchs, F., Miller, S.A., 2014. Seismic activity of the Nevados de Chillán volcanic complex after the 2010 Mw8.8 Maule, Chile, earthquake. J. Volcanol. Geotherm. Res. 283, 116–126. https://doi.org/10.1016/j.jvolgeores.2014.06.013.

Feigl, K.L., Le Mével, H., Tabrez Ali, S., Córdova, L., Andersen, N.L., DeMets, C., Singer, B.S., 2014. Rapid uplift in Laguna del Maule volcanic field of the Andean Southern Volcanic zone (Chile) 2007–2012. Geophys. J. Int. 196 (2), 885–901. https://doi.org/10.1093/gji/ggt438.

Global Volcanism Program, 2013. In: Venzke, E. (Ed.), Nevados de Chillán (357070) in Volcanoes of the World, v. 4.10.1 (29 Jun 2021). Smithsonian Institution. Downloaded 20 Jul 2021. https://volcano.si.edu/volcano.cfm?vn=357070.

Lundgren, P., Nikkhoo, M., Samsonov, S.V., Milillo, P., Gil-Cruz, F., Lazo, J., 2017. Source model for the Copahue volcano magma plumbing system constrained by InSAR surface deformation observations. J. Geophys. Res. Solid Earth 122 (7), 5729–5747. https://doi.org/10.1002/2017JB014368.

Mee, K., Tuffen, H., Gilbert, J.S., 2006. Snow-contact volcanic facies and their use in determining past eruptive environments at Nevados de Chillán volcano, Chile. Bull. Volcanol. 68, 363–376. https://doi.org/10.1007/s00445-005-0017-6.

Moussallam, Y., Bani, P., Schipper, C.I., Cardona, C., Franco, L., Barnie, T., Oppenheimer, C., 2018. Unrest at the Nevados de Chillán volcanic complex: a failed or yet to unfold magmatic eruption? Volcanica. https://doi.org/10.30909/vol.01.01.1932.

Moussallam, Y., Barnie, T., Amigo, Á., Kelfoun, K., Flores, F., Franco, L., Toloza, V., 2021. Monitoring and forecasting hazards from a slow growing lava dome using aerial imagery, tri-stereo Pleiades-1A/B imagery and PDC numerical simulation. Earth Planet. Sci. Lett. 564, 116906 https://doi.org/10.1016/j.epsl.2021.116906.

Naranjo, J.A., Lara, L.E., 2004. August-September 2003 small vulcanian eruption at the Nevados de Chillán Volcanic complex (36° 50'S), Southern Andes (Chile). Rev. Geol. Chile 31 (2), 359–366. https://doi.org/10.4067/S0716-02082004000200011.

Naranjo, J.A., Moreno, H., 2009. Reciente erupción en el Complejo Volcánico Nevados de Chillán, Región del Biobío. In: XII Congreso Geológico Chileno, Santiago, Actas (Vol. 3, p. 016), abstract.

Naranjo, J.A., Stern, C.R., 1998. Holocene explosive activity of Hudson Volcano, southern Andes. Bull. Volcanol. 59 (4), 291–306. https://doi.org/10.1007/s004450050193.

Okada, Y., 1985. Surface deformation due to shear and tensile faults in a half-space. Bull. Seismol. Soc. Am. 75 (4), 1135–1154. https://doi.org/10.1785/BSSA0750041135.

Orozco, G., Jara, G., Bertin, D., 2016. Peligros del Complejo Volcánico Nevados de Chillán, Región del Biobío. In: Servicio Nacional de Geología y Minería, Carta Geológica de Chile, Serie Geología Ambiental, 28, p. 34p.

OVDAS report, 2021. retrieved from: *http://sitiohistorico.sernageomin.cl/volcan.php?iId=32* (consulting date October 25).

Petit-Breuilh, M.E., 1995. The volcanic history of Nevados de Chillán volcano, Chile. In: British Geological Survey Technical Report WC/95/86, Nottingham, UK.

Pritchard, M.E., Simons, M., Rosen, P.A., Hensley, S., Webb, F.H., 2002. Co-seismic slip from the 1995 July 30 M_w=8.1 Antofagasta, Chile, earthquake as constrained by InSAR and GPS observations. Geophys. J. Int. 150 (2), 362–376. https://doi.org/10.1046/j.1365-246X.2002.01661.x.

Pritchard, M.E., Jay, J.A., Aron, F., Henderson, S.T., Lara, L.E., 2013. Subsidence at southern Andes volcanoes induced by the 2010 Maule, Chile earthquake. Nat. Geosci. 6 (8), 632–636. https://doi.org/10.1038/ngeo1855.

Radic, J.P., 2010. Las cuencas cenozoicas y su control en el volcanismo de los Complejos Nevados de Chillán y Copahue-Callaqui (Andes del Sur, 36–39°S). Andean Geol. 37 (1), 220–246. https://doi.org/10.4067/S0718-71062010000100009.

Ramos, V.A., Barbieri, M., 1989. El volcanismo cenozoico de Huantraico: Edad y relaciones isotópicas iniciales, provincia de Neuquén. Rev. Asoc. Geol. Argent. 43 (2), 210–223.

Ramos, V.A., Folguera, A., 2005. Tectonic evolution of the Andes of Neuquén: Constraints derived from the magmatic are and foreland deformation. In: A Case Study in Sequence Stratigraphy and Basin Dynamics, Geol. Soc. London, Spec. Publ, 252, pp. 15–35. https://doi.org/10.1144/GSL.SP.2005.252.01.02.

Sandwell, D., Mellors, R., Tong, X., Wei, M., Wessel, P., 2011a. Open radar interferometry software for mapping surface deformation. Eos Trans. AGU 92 (28). https://doi.org/10.1029/2011EO280002.

Sandwell, D., Mellors, R., Tong, X., Wei, M., Wessel, P., 2011b. GMTSAR: An InSAR Processing System Based on Generic Mapping Tools. Scripps Institution of Oceanography, UC San Diego. Retrieved from: http://escholarship.org/uc/item/8zq2c02m.

Singer, B.S., Andersen, N.L., Le Mével, H., Feigl, K.L., DeMets, C., Tikoff, B., Vazquez, J., 2014. Dynamics of a large, restless, rhyolitic magma system at Laguna del Maule, southern Andes, Chile. GSA Today 24 (12), 4–10. https://doi.org/10.1130/GSATG216A.1.

Stanton-Yonge, A., Griffith, W.A., Cembrano, J., St. Julien, R., Iturrieta, P., 2016. Tectonic role of margin-parallel and margin-transverse faults during oblique subduction in the Southern Volcanic Zone of the Andes: Insights from Boundary Element Modeling. Tectonics 35 (9), 1990–2013. https://doi.org/10.1002/2016TC004226.

Tymofyeyeva, E., Fialko, Y., 2015. Mitigation of atmospheric phase delays in InSAR data, with application to the eastern California shear zone. J. Geophys. Res. Solid Earth 120 (8), 5952–5963. https://doi.org/10.1002/2015JB011886.

Wessel, Paul, Smith, Walter, H.F., 1998. New, improved version of generic mapping tools released. Eos. Transactions American Geophysical Union 79 (47), 579. https://doi.org/10.1029/98EO00426.

Wright, T., Fielding, E., Parsons, B., 2001. Triggered slip: observations of the 17 August 1999 Izmit (Turkey) earthquake using radar interferometry. Geophys. Res. Lett. 2001 (28), 1079–1082. https://doi.org/10.1016/S0012-821X(99)00186-7.

Xu, X., Sandwell, D.T., Tymofyeyeva, E., González-Ortega, A., Tong, X., 2017. Tectonic and anthropogenic deformation at the Cerro Prieto geothermal step-over revealed by Sentinel-1A InSAR. IEEE Trans. Geosci. Remote Sens. 55 (9), 5284–5292. https://doi.org/10.1109/TGRS.2017.2704593.